

A study of the massive star forming region M8 using *Spitzer* IRAC images

Lokesh Kumar Dewangan^{1*}, & B.G. Anandarao^{1†}

¹*Astronomy & Astrophysics Division, Physical Research Laboratory, Navrangpura, Ahmedabad 380 009, India.*

ABSTRACT

Spitzer IRAC images (3.6, 4.5, 5.8 and 8.0 μm) and photometry of the star forming region M8 are presented. IRAC photometry reveals ongoing star formation in the M8 complex, with 64 Class 0/I and 168 Class II sources identified in several locations in the vicinity of sub-mm gas cores/clumps. Nearly 60% of these YSOs occur in about 7 small clusters. The spatial surface density of the clustered YSOs is determined to be about 10-20 YSOs/pc². Fresh star formation by the process of “collect and collapse” might have been triggered by the expanding HII regions and winds from massive stars. IRAC ratio images are generated and studied in order to identify possible diagnostic emission regions in M8. The image of 4.5 μm /8.0 μm reveals Br α counterpart of the optical Hourglass HII region, while the ratio 8.0 μm /4.5 μm indicates PAH emission in a cavity-like structure to the east of the Hourglass. The ratio maps of 3.6 μm /4.5 μm , 5.8 μm /4.5 μm and 8.0 μm /4.5 μm seem to identify PAH emission regions in the sharp ridges and filamentary structures seen East to West and NE to SW in M8 complex.

Key words: stars: formation – stars: pre-main-sequence – stars: winds and outflows – infrared: ISM – ISM: HII Regions – ISM: Individual: M8

1 INTRODUCTION

Messier 8 (M8), the Lagoon Nebula (or NGC 6523) is a well known galactic HII region (comprehensively reviewed in Tothill et al. (2008), and the references therein) situated at a distance of 1.25 kpc (Arias et al. 2006) in Sagittarius-Carina spiral arm of the Galaxy. The core of M8 contains a spectacular blister-type HII region, called the Hourglass nebula, ionized by the O7.5 V star Herschel 36 (Her 36) (Woolf 1961). The HII region is embedded within a giant molecular cloud that extends eastwards to the young star cluster NGC 6530 of age 2×10^6 yrs (Lada et al. 1976). While Her 36 is responsible for the Hourglass and the ionised bubble surrounding it, the other early type stars in M8 complex, 9 Sgr (O4 V(f)) and HD165052(O6.5V+O7.5V) are believed to account for the ionised regions east of the central core/bubble (Goudis 1976; Lada et al. 1976; Lynds & O’Neil 1982; Woodward et al. 1986). Allen (1986) discovered a few near-IR sources in the vicinity of Her 36, designated by Woodward et al. (1990) as KS 1 to KS 5. From a high resolution near-IR study, Arias et al. (2006, 2007) found the existence of a very young star cluster around Her 36, having an age of $\sim 10^6$ yrs. Barba & Arias (2007) discovered a number of HH objects in M8, which confirms

by implication, the existence of very young stars undergoing the accretion phase of formation. Narrow-band imaging by the Hubble Space Telescope (HST) revealed the presence of proplyds in the neighbourhood of Her 36 (Stecklum et al. 1998). The core of M8 is detected by the Mid-course Space Experiment (MSX) in mid-infrared as a luminous extended source (Crowther & Conti 2003). Color composite map of M8 in mid-infrared bands of *Spitzer* Infrared Array Camera (IRAC) shows a ridge extending in east-west direction to the south-east of the Hourglass (Tothill et al. 2008). There appear also a number of filamentary structures extending in the NE-SW direction to the east of Her 36 or the Hourglass. Among the new compact star forming regions in the M8 complex, M8E stands out with its compact HII region powered by an early B type star (M8E-Radio) (Lada et al. 1976; Wright et al. 1977; Brand & Zealey 1978; Mitchell et al. 1991; Linz et al. 2009). White et al. (1997) discovered very intense CO line emission in mm and sub-mm wavelength regions from the central core of M8. Later, from a larger survey in mm and sub-mm continuum and CO lines, Tothill et al. (2002) found bright rims and dark lanes stretching in the east-west direction. White et al. (1997) found from CO (J=3–2) line observations a loose bipolar structure extending NW-SE from Her 36; while Stecklum et al. (1995) found the presence of a jet-like object very close to Her 36. These observations provide evidence for outflow activity around Her 36 region. As for the spectral di-

* lokeshd@prl.res.in

† anand@prl.res.in

agnostics in the infrared region, Woodward et al. (1986) detected Br γ (2.17 μm), Br α (4.05 μm) as well as P β (3.03 μm) and the 3.28 μm polycyclic aromatic hydrocarbons (PAH) emission to the west of Her 36. Burton (2002) observed H $_2$ 1–0 S(1) line at 2.12 μm near the Hourglass/Her 36 region attributed primarily to shock-excited molecular gas; but UV excitation can not be ruled out.

The M8 region seems to be quite complex and very interesting, owing to the presence of stellar winds and expanding HII region bubbles from massive stars, which can trigger fresh star formation by sweeping up and compressing the local dense interstellar matter. The afore-mentioned near-IR surveys studied the regions around Her 36 and NGC 6530, leaving the ridge regions far-east and south-east of Her 36 relatively under-explored in near-IR (except 2MASS survey) and mid-IR regions (except MSX survey). In view of this, we wish to examine in detail the extended region of M8 in the near-/mid-infrared images provided by *Spitzer*, which are so far not looked into.

Spitzer IRAC provides an opportunity with an unprecedented high spatial resolution in thermal infrared wavelength regime that is very useful in identifying embedded sources in massive star forming regions. IRAC has four wavelength bands (with $\lambda_{eff}/\Delta\lambda$, 3.55/0.75, 4.49/1.0, 5.73/1.43 and 7.87/2.91 μm) which include molecular emissions such as those from H $_2$ and PAH molecules, as well as recombination lines from hydrogen. The aims of the present study are to identify the embedded sources using the IRAC bands in order to classify the different stages of their evolution; to use ratio maps of the four IRAC bands in order to identify possible H $_2$, PAH or H emission regions, following the suggestions of Smith & Rosen (2005) and Povich et al. (2007).

In Section 2, we describe the data used for the present study and the analysis tasks utilised. Section 3 presents the results and discussion on *Spitzer* IRAC photometry of embedded sources associated with M8 complex. In this section, we also present the results and discussion on the ratio maps. In Section 4, we give the conclusions.

2 SPITZER IRAC DATA ON MESSIER 8 AND DATA REDUCTION

The *Spitzer* Space Telescope IRAC observation of M8 were obtained by Spitzer Science Center (SSC) on 16 September 2005 and Basic Calibrated Data (BCDs) images were processed by SSC using software version S14.0.0 for all four bands (see Fazio et al. (2004), for details on the IRAC instrument). The observations relevant for M8 region were taken in High Dynamic Range (HDR) mode with 12s integration time in all filters. These observations were a part of the project entitled, “Spitzer Follow-up of HST Observations of Star Formation in H II Regions” (Program id 20726; PI: Jeff Hester). The IRAC archival images of M8 were obtained by us on 8 April 2009 from the Spitzer public archive, using ‘leopard’ software. The BCD images were processed for ‘jailbar’ removal, saturation and ‘muxbled’ correction before making the final mosaic using Mopex and IDL softwares (Makovoz & Marleau 2005). A pixel ratio (defined as the ratio of the area formed by the original pixel scale, 1.22 arcsec/px, to that of the mosaiced pixel scale) of 2 was adopted for making the mosaic (which gives a mosaic pixel

scale of 0.86 arcsec/pixel)¹. Using these procedures, a total number of 320 BCD images of 5.2×5.2 arcmin² were mosaiced to make a final image of 42.5×30.0 arcmin² in each of the four bands. Aperture photometry was performed on the mosaic with 2.8 pixel aperture and sky annuli of 2.8 and 8.5 pixels using APPHOT task in IRAF package. The zero points for these apertures (including aperture corrections) are, 17.08, 17.30, 16.70 and 15.88 mag for the 3.6, 4.5, 5.8, 8.0 μm bands, here onwards called as Ch1, Ch2, Ch3 and Ch4 respectively (see Reach et al. (2005)). The photometric uncertainties vary between 0.01 to 0.25 for the four channels, with Ch3 and Ch4 on the higher side.

We have looked into the 2MASS archives (Skrutskie et al. 2006) as well as published literature for JHK photometric data on sources identified from IRAC and succeeded in extracting for nearly half of them. From 2MASS archives, we have considered only the data with tags of A, B or C (or a S/N of ≥ 5) in all the JHK bands.

3 RESULTS AND DISCUSSION

We divide the results and discussion into two subsections: one in which we discuss the IRAC photometry and the pre-main-sequence sources or the young stellar objects (YSOs) detected and their possible formation scenario; and the second in which we describe the ratio maps produced from IRAC images and discuss possible interpretations and their implications.

3.1 IRAC Photometry

Fig 1 shows the IRAC Ch4 (8 μm) image of $\sim 42.5 \times 30.0$ arcmin² of M8 region with Her 36 situated near the centre. Following earlier workers, M8 may be divided into a few distinct regions for convenience (see Fig 1): the Her 36 region comprising of the bubble-like structure around Her 36 with the massive stars 9 Sgr and HD 164816 forming the eastern/north-eastern bounds; the central ridge that includes filamentary structures seen in the NE-SW direction; the massive star HD 164906 and the cluster NGC 6530; the east-west ridge region consisting of the finger-like filamentary structures starting from far-east to the south of Her 36; and the compact young cluster region M8E.

Using the [3.6]-[4.5] vs [5.8]-[8.0] colour-colour diagrams, Allen et al. (2004) and Megeath et al. (2004) formulated division criteria for various pre-main-sequence classes such as Classes 0/I, I, II and III. These criteria have since been refined by several authors (e.g., Harvey et al. (2006, 2007); Gutermuth et al. (2008, 2009); Evans et al. (2009) and the references therein), in order to account for possible contaminations from broad-line AGNs, PAH-emitting galaxies, shocked emission blobs/knots and unresolved PAH-emission-contaminated apertures, which may lead to wrongful identifications of YSOs. We used the updated criteria given clearly in the Appendix A of Gutermuth et al. (2009) to delineate the PMS sources. The total number of point sources identified that are common to all the four IRAC

¹ see <http://ssc.spitzer.caltech.edu/postbcd/doc/mosaiker.pdf>

Table 1. *Spitzer* IRAC 4-channel photometry (in mag) of the Class 0/I YSOs identified in M8 (see text for details); the numbers in the last column refer to: 1. 2MASS; 2. Arias et al. (2006); 3. Arias et al. (2007)

Object	RA [2000]	Dec [2000]	Ch1	Ch2	Ch3	Ch4	α_{IRAC}	H	J-H	H-K	NIR Ref.
1	18:02:25.56	-24:32:41.7	12.63	11.88	10.87	9.76	0.51				
2	18:02:29.28	-24:08:15.8	5.79	5.12	4.41	3.45	-0.15	9.46	3.16	1.96	1
3	18:02:42.07	-24:19:13.2	12.19	10.63	9.54	8.62	1.20				
4	18:02:42.97	-24:23:25.5	11.28	10.13	9.28	8.33	0.51				
5	18:02:49.71	-24:22:26.6	11.36	9.90	9.13	8.82	-0.01				
6	18:02:52.85	-24:20:46.6	11.52	10.27	9.54	8.85	0.15				
7	18:02:53.21	-24:20:17.3	8.91	8.31	7.82	5.94	0.49	9.79	0.16	0.19	1
8	18:03:06.89	-24:20:57.6	11.08	10.29	9.52	8.24	0.40				
9	18:03:06.99	-24:21:20.1	8.78	7.87	6.86	5.94	0.46				
10	18:03:11.64	-24:11:57.0	6.63	5.57	4.28	3.41	0.94				
11	18:03:12.28	-24:33:30.5	8.12	7.13	6.16	5.88	-0.22				
12	18:03:25.59	-24:21:08.3	10.88	10.21	9.42	8.55	-0.13				
13	18:03:27.38	-24:21:04.0	11.81	9.98	9.08	8.63	0.69				
14	18:03:29.22	-24:21:49.9	10.34	9.89	9.05	7.80	0.13	13.27	1.44	1.08	1
15	18:03:30.84	-24:20:03.1	11.73	9.94	8.63	7.36	2.12				
16	18:03:35.58	-24:22:04.6	11.86	10.75	9.51	7.37	2.31				
17	18:03:36.21	-24:18:13.7	9.87	8.67	7.91	7.11	0.27				
18	18:03:36.28	-24:17:51.1	8.75	7.66	6.68	5.53	0.85				
19	18:03:37.05	-24:22:31.6	10.34	9.36	8.25	7.06	0.96	13.87	1.13	0.98	1,2
20	18:03:37.41	-24:13:56.9	4.64	4.04	3.09	2.43	-0.21	6.83	1.95	1.28	1
21	18:03:37.74	-24:25:30.3	11.24	10.18	9.47	8.17	0.61				
22	18:03:38.31	-24:33:59.8	11.71	10.59	9.67	8.56	0.75				
23	18:03:38.65	-24:22:24.3	9.00	7.90	6.96	5.22	1.45	12.52	1.01	0.92	1,2,3
24(KS 1)	18:03:40.37	-24:22:38.6	6.19	5.29	4.46	2.51	1.34	10.61	1.63	1.08	2
25(Her 36)	18:03:40.43	-24:22:43.6	5.42	4.72	3.86	2.27	0.79	7.45	0.49	0.54	1,2
26(KS 4)	18:03:41.50	-24:22:44.3	9.36	8.58	—	—	—	12.99	2.17	1.46	2
27	18:03:44.95	-24:16:08.7	11.13	10.66	9.88	8.58	0.13				
28	18:03:45.16	-24:23:25.0	8.88	8.20	7.54	6.24	0.18	11.36	1.30	0.92	2,3
29	18:03:47.05	-24:25:37.4	8.45	7.86	6.95	6.08	-0.05	11.81	1.74	1.37	1
30	18:03:47.37	-24:18:44.4	8.73	8.16	7.29	6.33	-0.03				
31	18:03:47.47	-24:25:34.5	8.73	7.87	6.99	6.13	0.16				
32	18:03:48.44	-24:26:32.0	9.77	8.64	7.75	7.29	0.00				
33	18:03:48.47	-24:25:58.6	10.47	9.09	8.40	7.66	0.28				
34	18:03:50.26	-24:22:23.4	10.03	9.54	8.95	7.80	-0.28	11.96	0.85	0.56	1
35	18:03:54.23	-24:25:33.3	10.15	9.40	8.28	6.88	0.98	13.27	1.72	1.04	1
36	18:04:05.11	-24:16:42.3	10.80	10.04	9.56	8.43	-0.19	12.59	0.83	0.32	1
37	18:04:08.81	-24:27:27.5	10.36	9.54	8.90	8.11	-0.28				
38	18:04:10.55	-24:26:56.1	9.00	8.32	7.84	6.59	-0.13	11.10	0.99	0.62	1,3
39	18:04:11.03	-24:27:20.5	11.66	9.48	8.11	7.10	2.29				
40	18:04:11.07	-24:21:31.5	6.56	5.72	4.83	3.96	0.17				
41	18:04:11.08	-24:26:54.2	10.07	8.46	7.35	6.39	1.33				
42	18:04:17.06	-24:28:10.9	11.32	10.62	9.87	8.72	0.15	13.67	1.13	0.65	1
43	18:04:20.09	-24:29:14.7	5.56	4.33	2.95	2.77	0.46				
44	18:04:20.74	-24:28:22.1	10.06	9.35	8.57	7.50	0.11	13.03	1.87	1.20	1
45	18:04:20.95	-24:21:07.9	11.40	10.78	10.44	9.01	-0.19	13.10	1.06	0.56	1
46	18:04:21.24	-24:28:03.5	9.86	9.45	8.60	7.39	0.07	12.49	1.31	0.88	1,3
47	18:04:21.63	-24:11:26.3	9.33	8.68	7.92	7.08	-0.23	12.61	2.35	1.51	1
48	18:04:21.70	-24:21:14.6	11.47	10.98	10.29	9.05	-0.04				
49	18:04:23.98	-24:21:27.0	9.19	8.79	8.30	6.58	0.12	9.25	0.07	0.03	1
50	18:04:24.31	-24:20:59.7	9.45	9.17	8.49	6.82	0.20	9.83	0.04	0.01	1
51	18:04:26.52	-24:29:00.3	9.72	9.30	8.59	7.36	-0.09	11.82	1.04	0.50	1
52	18:04:28.09	-24:22:41.8	11.25	10.82	10.10	8.89	-0.10				
53	18:04:28.90	-24:14:02.6	8.46	8.05	7.30	6.06	-0.04	10.19	0.42	0.32	1
54	18:04:30.74	-24:28:45.6	6.75	6.02	5.34	4.27	-0.01	10.52	1.99	1.49	1
55	18:04:35.78	-24:28:35.6	9.03	8.44	7.71	6.74	-0.19				
56	18:04:40.67	-24:12:16.9	11.06	10.66	9.96	8.78	-0.19	13.01	1.06	0.52	1
57	18:04:44.19	-24:15:25.1	10.67	10.25	9.57	8.32	-0.11	12.01	0.91	0.37	1
58	18:04:47.09	-24:27:55.4	9.05	8.08	7.36	6.51	0.04				
59	18:04:48.42	-24:27:53.8	10.99	10.66	9.92	8.64	-0.09				
60	18:04:50.37	-24:14:25.8	5.02	4.27	3.29	2.31	0.32				

Table 1 – *continued*

Object	RA [2000]	Dec [2000]	Ch1	Ch2	Ch3	Ch4	α_{IRAC}	H	J-H	H-K	NIR Ref.
61	18:04:50.62	-24:25:42.2	8.73	8.11	7.67	5.87	0.36	10.16	0.29	0.43	3
62	18:04:51.13	-24:26:33.7	9.48	9.03	8.52	6.93	0.05	12.68	1.95	1.13	1
63	18:04:56.77	-24:27:16.4	10.30	9.24	8.44	7.56	0.27				
64	18:04:58.82	-24:26:24.1	9.54	8.47	7.82	6.89	0.13				
65	18:05:00.47	-24:13:26.8	9.51	8.88	8.25	6.94	0.08	10.89	0.62	0.37	1

Table 2. *Spitzer* IRAC 4-channel photometry (in mag) of the Class II YSOs identified in M8 (see text for details); the numbers in the last column refer to: 1. 2MASS; 2. Arias et al. (2006); 3. Arias et al. (2007)

Object	RA [2000]	Dec [2000]	Ch1	Ch2	Ch3	Ch4	α_{IRAC}	H	J-H	H-K	NIR Ref.
1	18:02:23.78	-24:08:49.4	10.76	10.41	10.04	9.26	-1.13	12.29	0.94	0.42	1
2	18:02:24.95	-24:36:08.4	7.92	7.57	7.12	6.86	-1.59	9.59	2.31	1.02	1
3	18:02:25.98	-24:27:31.8	6.83	6.25	5.59	4.74	-0.42	11.46	3.65	2.14	1
4	18:02:27.52	-24:22:52.9	8.12	7.53	6.69	6.49	-0.88				
5	18:02:27.65	-24:11:38.0	11.53	11.20	10.43	9.70	-0.66				
6	18:02:29.49	-24:24:53.7	10.58	10.05	9.81	8.97	-1.07	12.71	1.08	0.69	1
7	18:02:36.33	-24:21:07.9	8.10	7.83	7.23	6.94	-1.43	11.15	3.46	1.78	1
8	18:02:37.34	-24:16:24.4	10.40	9.98	9.55	8.86	-1.08	12.47	0.92	0.56	1
9	18:02:41.45	-24:10:35.3	8.26	7.91	7.36	7.20	-1.56	10.85	3.13	1.48	1
10	18:02:41.65	-24:33:55.0	7.92	7.55	6.94	6.11	-0.73	9.60	2.07	0.93	1
11	18:02:42.67	-24:17:18.9	6.34	6.06	5.42	4.88	-1.09				
12	18:02:43.91	-24:15:23.1	10.71	10.26	9.85	9.03	-0.93	12.55	0.77	0.56	1
13	18:02:45.65	-24:13:49.7	8.47	7.92	7.53	7.24	-1.44	10.85	2.89	1.47	1
14	18:02:48.85	-24:21:08.8	9.56	9.24	8.87	7.88	-0.92	12.34	0.84	0.62	1
15	18:02:49.10	-24:28:15.8	7.32	6.91	6.47	6.13	-1.46	10.59	2.99	1.62	1
16	18:02:49.15	-24:08:52.3	6.50	6.04	5.73	4.96	-1.12	9.75	2.88	1.59	1
17	18:02:49.33	-24:11:19.0	5.80	5.34	5.00	4.63	-1.51	9.30	2.55	1.47	1
18	18:02:50.81	-24:17:56.6	9.95	9.29	9.03	8.29	-1.02	12.50	1.43	0.95	1
19	18:02:50.95	-24:22:20.1	10.65	10.21	9.83	8.82	-0.76				
20	18:02:51.10	-24:19:23.4	9.59	9.20	8.84	8.02	-1.05	12.64	1.32	0.95	1
21	18:02:51.12	-24:16:57.2	5.29	4.20	3.38	3.18	-0.43				
22	18:02:51.15	-24:18:07.9	10.45	9.78	9.50	8.74	-0.96	12.95	0.96	0.71	1
23	18:02:51.39	-24:17:13.3	9.48	9.15	8.59	8.26	-1.38				
24	18:02:52.47	-24:18:44.7	8.56	8.14	7.64	6.78	-0.79	10.72	0.90	0.75	1
25	18:02:53.83	-24:20:19.8	9.22	8.68	8.60	7.92	-1.45				
26	18:02:53.96	-24:20:11.3	9.97	9.51	9.16	8.41	-1.09	12.61	1.29	1.00	1
27	18:02:54.30	-24:20:56.5	8.85	8.35	8.01	7.20	-0.99	11.23	0.92	0.77	1
28	18:02:54.72	-24:19:56.9	9.57	9.14	8.75	8.47	-1.57				
29	18:02:56.79	-24:23:34.8	10.17	9.89	9.62	8.98	-1.49	12.32	2.42	1.10	1
30	18:02:56.88	-24:35:40.7	8.08	7.79	7.28	7.04	-1.59	10.20	2.84	1.29	1
31	18:03:01.50	-24:27:47.1	10.53	10.13	9.47	8.48	-0.45	12.93	1.70	0.90	1
32	18:03:05.14	-24:31:54.2	5.57	5.16	4.61	3.81	-0.80				
33	18:03:06.56	-24:32:13.1	5.60	4.96	4.44	3.56	-0.53	8.46	2.91	1.63	1
34	18:03:09.96	-24:33:50.4	8.10	7.50	6.97	6.67	-1.19	10.79	2.63	1.38	1
35	18:03:10.31	-24:26:59.5	6.49	5.89	5.43	4.59	-0.69	10.50	2.93	1.92	1
36	18:03:17.69	-24:20:53.2	10.74	10.25	9.77	8.93	-0.77	12.20	1.08	0.45	1
37	18:03:18.30	-24:25:58.7	8.19	7.44	6.70	6.20	-0.53	10.30	2.58	1.45	1
38	18:03:20.03	-24:20:20.4	10.45	10.21	9.81	9.05	-1.21	12.45	2.12	0.99	1
39	18:03:20.53	-24:30:29.8	5.27	5.09	4.69	4.18	-1.54	8.31	2.35	1.44	1
40	18:03:23.06	-24:23:41.8	7.03	6.61	6.22	5.82	-1.45	11.43	2.97	1.82	1
41	18:03:23.09	-24:21:33.1	9.80	9.53	8.88	8.65	-1.42				
42	18:03:24.06	-24:21:23.3	8.58	7.94	7.17	6.95	-0.91				
43	18:03:25.06	-24:19:02.2	8.07	7.72	7.07	6.93	-1.44	10.34	3.06	1.45	1
44	18:03:25.12	-24:21:28.4	11.06	10.06	9.49	8.85	-0.36				
45	18:03:26.71	-24:22:11.3	8.91	8.68	8.27	7.22	-0.88				
46	18:03:34.15	-24:24:59.7	8.17	7.83	7.19	7.07	-1.50	10.50	2.96	1.44	1
47	18:03:34.74	-24:18:53.7	6.44	6.20	5.68	5.32	-1.50	10.57	3.94	2.21	1
48	18:03:35.86	-24:09:11.9	9.61	8.85	8.82	7.90	-1.04	11.63	0.91	0.64	1
49	18:03:36.29	-24:09:48.2	6.11	5.74	5.31	4.38	-0.85	10.88	2.82	1.78	1
50	18:03:36.68	-24:10:32.6	8.59	8.39	8.00	7.52	-1.58	10.50	2.04	0.86	1

Table 2 – continued

Object	RA [2000]	Dec [2000]	Ch1	Ch2	Ch3	Ch4	α_{IRAC}	H	J-H	H-K	NIR Ref.
51	18:03:36.84	-24:24:15.1	10.23	9.71	9.39	8.20	-0.58	12.26	0.89	0.37	1
52	18:03:37.32	-24:22:46.9	9.01	8.44	7.99	6.88	-0.44	11.47	1.34	0.66	2
53	18:03:38.49	-24:22:31.7	8.81	8.11	7.57	6.63	-0.38	10.80	1.22	0.80	1,2
54	18:03:38.81	-24:08:58.8	5.43	5.08	4.59	3.86	-1.02	8.58	2.92	1.55	1
55	18:03:39.05	-24:28:10.8	8.16	7.74	7.09	6.81	-1.23	9.97	2.41	1.11	1
56	18:03:39.38	-24:25:24.2	9.54	9.06	8.54	7.38	-0.37	11.85	1.14	0.69	1
57	18:03:40.23	-24:22:03.8	9.54	9.15	8.74	7.84	-0.90	11.66	1.31	0.63	1
58	18:03:40.24	-24:29:08.2	5.05	4.51	3.84	2.93	-0.38	8.93	2.76	1.92	1
59	18:03:40.33	-24:25:05.2	10.39	9.78	9.54	8.58	-0.86	12.25	1.04	0.54	1
60	18:03:40.74	-24:23:16.3	8.67	8.29	7.83	6.87	-0.77	11.24	1.10	0.80	1,2,3
61	18:03:41.05	-24:25:45.6	8.54	8.21	7.73	7.23	-1.30				
62	18:03:42.26	-24:23:22.4	9.68	9.10	8.70	7.76	-0.69	12.48	1.40	0.94	1,2
63	18:03:42.89	-24:16:26.4	8.17	7.79	7.21	7.03	-1.47	9.83	2.26	1.07	1
64	18:03:43.09	-24:21:29.6	8.49	8.29	7.87	7.08	-1.20	10.84	2.75	1.25	1
65	18:03:43.29	-24:28:07.1	8.14	7.90	7.19	7.09	-1.52	10.13	2.62	1.29	1
66	18:03:45.07	-24:22:05.6	8.61	8.45	8.15	6.37	-0.30	9.13	0.11	0.10	1,2
67	18:03:47.93	-24:18:02.1	9.05	8.45	8.00	7.37	-0.94	12.65	1.94	1.43	1
68	18:03:49.38	-24:26:14.6	8.47	8.04	7.42	7.27	-1.40				
69	18:03:49.61	-24:22:09.3	10.85	10.36	9.99	8.85	-0.59	12.65	0.99	0.42	1
70	18:03:50.73	-24:20:13.3	9.81	9.57	9.31	8.44	-1.29				
71	18:03:50.79	-24:21:10.9	6.46	6.14	5.61	4.60	-0.68	9.21	0.86	0.85	1,3
72	18:03:51.65	-24:28:26.7	9.51	9.21	8.91	8.12	-1.25	11.58	0.80	0.64	1
73	18:03:53.05	-24:14:51.6	8.17	7.59	7.17	6.89	-1.38				
74	18:03:57.82	-24:20:51.3	10.21	9.67	9.43	8.52	-0.97				
75	18:03:57.84	-24:25:34.9	6.09	5.54	5.09	4.25	-0.76	8.84	0.94	0.83	1
76	18:03:58.29	-24:16:49.3	9.95	9.26	8.95	8.10	-0.81	12.24	1.02	0.71	1,3
77	18:03:58.54	-24:24:58.8	9.66	9.31	8.90	8.18	-1.14	11.24	0.87	0.41	1
78	18:03:59.27	-24:23:08.2	9.01	8.79	8.59	7.76	-1.44	11.16	1.24	0.93	1
79	18:04:01.13	-24:22:35.6	10.49	10.30	9.93	8.96	-1.06	12.33	2.19	0.99	1
80	18:04:03.10	-24:25:19.5	9.53	9.17	8.70	7.60	-0.63	11.72	0.66	0.58	1
81	18:04:04.65	-24:08:49.8	8.03	7.69	7.13	6.92	-1.51	9.89	2.31	1.12	1
82	18:04:07.89	-24:26:06.3	10.69	10.27	9.69	8.55	-0.37				
83	18:04:08.11	-24:20:55.6	10.90	10.39	10.04	9.04	-0.75	13.03	1.00	0.47	1
84	18:04:08.47	-24:20:49.5	10.76	10.44	10.08	8.93	-0.76	12.39	0.93	0.38	1
85	18:04:09.94	-24:25:32.7	9.72	9.27	9.02	8.20	-1.15	11.15	0.94	0.38	1
86	18:04:10.19	-24:25:49.6	9.09	8.62	8.20	7.27	-0.78	11.80	1.17	0.69	1
87	18:04:11.57	-24:28:42.1	12.10	11.85	11.11	10.95	-1.40				
88	18:04:11.99	-24:26:28.1	10.18	9.57	9.07	8.18	-0.57	11.81	0.96	0.43	1
89	18:04:12.48	-24:11:51.6	10.83	10.10	9.70	8.67	-0.44	12.83	1.00	0.73	1
90	18:04:12.52	-24:35:47.1	8.15	7.83	7.43	7.07	-1.58	9.39	2.02	0.81	1
91	18:04:13.10	-24:26:13.3	10.88	10.43	9.90	8.80	-0.46	12.38	0.99	0.43	1
92	18:04:15.75	-24:19:01.7	10.07	9.80	9.64	8.80	-1.43	11.71	0.80	0.41	1,3
93	18:04:15.77	-24:25:15.8	10.71	10.17	9.79	9.09	-1.02				
94	18:04:15.91	-24:18:46.2	10.05	9.35	9.12	8.48	-1.13	12.44	1.11	0.81	1,3
95	18:04:16.06	-24:27:57.4	10.05	9.70	9.34	8.79	-1.40				
96	18:04:16.14	-24:19:52.5	9.41	8.86	8.44	7.45	-0.63	11.45	0.92	0.62	1
97	18:04:16.41	-24:24:38.8	9.67	9.17	8.79	7.74	-0.67	11.88	1.10	0.78	1,3
98	18:04:16.93	-24:24:14.9	9.16	8.75	8.38	7.84	-1.33	10.96	0.70	0.38	1
99	18:04:17.42	-24:19:09.8	8.83	8.42	8.00	7.53	-1.34	11.37	1.57	0.98	1,3
100	18:04:17.89	-24:17:46.8	10.39	9.84	9.60	8.44	-0.69	12.02	0.94	0.57	1
101	18:04:19.09	-24:27:58.8	10.28	9.70	9.17	8.18	-0.46	12.43	1.20	0.73	1
102	18:04:19.31	-24:22:54.9	9.95	9.60	9.33	8.70	-1.42	11.50	0.94	0.47	1,3
103	18:04:19.58	-24:24:04.7	9.00	8.77	8.37	7.81	-1.44	11.79	1.48	1.16	1
104	18:04:19.87	-24:28:23.7	9.45	8.86	8.46	7.73	-0.91				
105	18:04:20.07	-24:22:48.2	10.58	10.26	9.66	8.51	-0.44	12.09	0.89	0.83	3
106	18:04:20.26	-24:20:24.8	10.14	9.79	9.41	8.65	-1.14	12.32	1.04	0.73	1
107	18:04:20.34	-24:24:34.6	10.75	9.93	9.51	9.07	-0.96				
108	18:04:20.52	-24:23:04.1	9.96	9.48	8.97	8.12	-0.73				
109	18:04:20.61	-24:23:01.1	10.24	9.89	9.45	8.47	-0.81				
110	18:04:20.82	-24:23:22.5	10.33	9.92	9.68	8.88	-1.22	12.46	1.05	0.83	1

Table 2 – *continued*

Object	RA [2000]	Dec [2000]	Ch1	Ch2	Ch3	Ch4	α_{IRAC}	H	J-H	H-K	NIR Ref.
111	18:04:21.01	-24:13:41.8	5.42	5.01	4.51	3.69	-0.85	8.69	2.32	1.39	1
112	18:04:21.11	-24:23:25.5	10.08	9.81	9.42	8.66	-1.20				
113	18:04:21.12	-24:20:47.7	10.46	10.24	9.84	8.79	-0.91				
114	18:04:21.19	-24:24:22.4	10.39	9.96	9.55	8.89	-1.13				
115	18:04:21.47	-24:23:19.1	9.46	9.16	8.62	7.94	-1.05				
116	18:04:21.69	-24:23:19.7	9.75	9.27	8.63	7.75	-0.51				
117	18:04:21.82	-24:22:15.6	10.84	10.58	10.09	9.03	-0.74	13.02	0.91	0.52	1
118	18:04:21.84	-24:16:26.2	9.83	9.50	9.27	8.23	-1.05	11.67	0.89	0.49	1
119	18:04:21.86	-24:11:37.5	10.57	10.24	9.80	8.53	-0.51	11.77	0.51	0.22	1
120	18:04:22.77	-24:22:09.7	8.53	8.09	7.65	6.87	-0.95	8.86	0.22	0.30	1
121	18:04:23.05	-24:24:15.2	10.12	9.88	9.27	8.94	-1.40				
122	18:04:23.54	-24:22:47.6	9.69	9.15	8.76	8.46	-1.45				
123	18:04:24.23	-24:16:25.2	9.95	9.53	9.04	8.29	-0.94	12.71	1.47	1.01	1
124	18:04:26.15	-24:22:45.1	6.73	6.24	5.77	5.03	-0.90	10.23	1.65	1.27	1
125	18:04:26.75	-24:22:42.0	11.17	10.85	10.35	9.08	-0.43	13.08	1.09	0.62	1
126	18:04:26.84	-24:23:23.5	9.07	8.71	8.44	7.71	-1.30	11.30	0.88	0.66	1
127	18:04:27.09	-24:21:06.8	10.84	10.37	10.16	9.07	-0.89	12.36	0.95	0.51	1
128	18:04:27.27	-24:20:57.0	9.41	9.06	8.82	8.23	-1.52	12.59	1.47	1.03	1
129	18:04:27.36	-24:14:27.3	9.84	9.38	8.74	8.05	-0.75	12.69	1.31	1.09	1
130	18:04:27.48	-24:07:31.1	8.03	7.76	7.19	6.85	-1.42				
131	18:04:28.03	-24:21:43.2	8.03	7.57	7.16	6.04	-0.59	7.97	-0.04	0.07	1
132	18:04:28.25	-24:25:48.0	10.14	9.76	9.39	8.62	-1.11				
133	18:04:28.66	-24:20:20.0	5.77	5.47	5.16	4.44	-1.33	8.19	2.12	1.18	1
134	18:04:29.67	-24:25:19.4	7.09	6.90	6.26	6.03	-1.52	10.36	2.07	1.31	1
135	18:04:29.93	-24:14:29.8	10.46	10.08	9.76	9.05	-1.24	12.67	1.13	0.63	1
136	18:04:30.59	-24:26:06.9	8.16	7.69	7.25	6.85	-1.33	10.29	1.94	1.00	1
137	18:04:31.07	-24:29:09.9	10.59	10.41	9.89	9.04	-1.00				
138	18:04:32.35	-24:19:28.1	10.07	9.53	9.07	8.02	-0.52	12.48	0.96	0.59	1
139	18:04:32.39	-24:27:55.2	10.33	9.95	9.61	8.82	-1.13	13.36	1.62	1.04	1
140	18:04:33.22	-24:27:18.0	9.68	9.02	8.77	8.17	-1.18	11.56	1.15	0.77	1
141	18:04:33.58	-24:21:54.8	8.70	8.45	7.81	6.89	-0.70	10.42	0.97	0.61	1
142	18:04:34.61	-24:09:02.0	5.30	4.66	4.23	3.43	-0.75	9.29	2.80	1.74	1
143	18:04:34.94	-24:22:51.9	10.70	10.27	9.92	8.84	-0.75	12.99	0.99	0.58	1
144	18:04:36.50	-24:19:13.7	10.23	9.73	9.38	8.96	-1.40				
145	18:04:38.90	-24:19:28.2	8.24	7.87	7.32	7.11	-1.49				
146	18:04:39.31	-24:32:24.4	5.64	5.25	4.61	3.77	-0.65	10.00	2.60	1.61	1
147	18:04:39.46	-24:27:09.2	10.46	9.99	9.57	8.65	-0.79	12.26	1.10	0.53	1
148	18:04:39.86	-24:23:05.2	9.55	9.05	8.53	7.57	-0.58	12.28	1.22	0.83	1
149	18:04:40.90	-24:17:10.8	9.29	9.01	8.71	8.15	-1.54	11.70	1.05	0.70	1,3
150	18:04:41.27	-24:15:44.9	5.14	4.58	4.14	3.83	-1.35	7.66	2.63	1.41	1
151	18:04:41.63	-24:26:31.8	8.11	7.49	7.02	6.71	-1.24	10.05	2.07	1.11	1
152	18:04:43.53	-24:27:38.7	8.40	7.76	7.22	6.46	-0.64	10.78	1.21	0.76	3
153	18:04:43.65	-24:27:59.1	10.26	9.86	9.63	9.00	-1.44	13.01	1.47	0.94	1
154	18:04:44.06	-24:19:39.7	10.48	10.02	9.75	8.99	-1.18	12.07	0.84	0.43	1
155	18:04:44.46	-24:10:17.5	10.15	9.85	9.64	8.85	-1.38				
156	18:04:46.41	-24:26:08.0	10.42	10.05	9.52	8.52	-0.65	12.54	1.13	0.53	1
157	18:04:48.05	-24:27:24.6	7.20	6.59	6.16	5.74	-1.18				
158	18:04:48.56	-24:26:40.7	8.89	8.46	8.04	7.29	-1.02	11.02	1.58	0.95	1,3
159	18:04:50.23	-24:27:59.4	10.40	10.09	9.36	8.82	-0.93				
160	18:04:51.53	-24:24:17.4	10.06	9.45	9.00	8.08	-0.61	12.28	1.21	0.61	1
161	18:04:51.57	-24:26:10.9	10.72	10.02	9.96	9.00	-1.01				
162	18:04:51.63	-24:25:15.8	10.37	9.88	9.40	8.91	-1.16	12.02	0.97	0.47	1
163	18:04:52.64	-24:27:30.8	10.72	10.42	9.67	8.99	-0.76	13.28	1.16	0.70	1
164	18:04:53.48	-24:26:08.7	8.45	7.91	7.21	6.66	-0.74				
165	18:04:54.08	-24:26:23.7	7.05	6.33	5.96	5.45	-1.06				
166	18:04:55.00	-24:27:18.1	9.15	8.77	8.29	7.42	-0.84	12.59	2.04	1.33	1
167	18:04:56.18	-24:09:00.9	8.16	7.78	7.55	6.98	-1.52	10.06	2.02	0.99	1
168	18:04:57.35	-24:20:48.4	4.49	4.30	3.58	3.28	-1.33				

bands is 3376; of these, 235 sources are found to be contaminations (1 PAH galaxy, 6 shocked emissions, 228 PAH aperture-contaminations), while there are 327 YSOs.

After removing the contaminants, we used the criteria based on the spectral index, $\alpha_\lambda (= \text{dlog}(\lambda F_\lambda)/\text{dlog}(\lambda))$, to classify the YSOs (numbering 327 as shown above) into different evolutionary classes (see e.g., Green et al. (1994); Smith (2004); Lada et al. (2006)). We followed Billot et al. (2010) in the classification of Class 0/I as sources whose α_{IRAC} is > -0.3 ; Class II as those having $-0.3 > \alpha_{IRAC} > -1.6$; and Class III as those having $-1.6 > \alpha_{IRAC} > -2.6$ (termed as sources with faint or anemic disks by Lada et al. (2006)). In applying these classifications to M8, we have not considered the flat-spectrum sources (e.g., Green et al. (1994)) as a separate class but included them in the Class 0/I, the sources with in-falling envelopes (see Billot et al. (2010)). The sources with $\alpha_{IRAC} < -2.6$ are taken as stars with purely photospheric emissions. With the α_{IRAC} classification, we obtain 64 Class 0/I, 168 Class II sources and 95 Class III sources. The rest of the sources, numbering 2814, are purely photospheric sources.

We then verified the selected sample of YSOs for possible interstellar extinction/reddening bias (see Muench et al. (2007) and the references therein). Muench et al. (2007) showed that only for very large values of A_v do sources, with α_{IRAC} ranges relevant here, get misclassified as YSOs. Such large values are seen only as intrinsic for YSOs as may be inferred from the H-K colour. Typically, we can identify the bias by comparing the ratio (N) of number of Class II sources to that of the Class 0/I, for different values of extinction and see if the ratio changes substantially (Guieu et al. 2009). In the case of M8, the visual extinction and the reddening (defined as the ratio of total to selective extinction, $R_v = A_v/E(B-V)$) varies from region to region; and a value of $A_v = 3.2$ was determined towards the Hourglass region for standard reddening ($R_v = 3.1$) (Arias et al. 2006; Tothill et al. 2008). For the present purpose, however, we compared the ratio N , for A_v values 0.0, 3.2 and 5.0. The ratio N remains at 2.63 with a Poisson error of ± 0.39 for A_v 0.0 and 3.2. For $A_v = 5.0$, we get $N = 2.73 \pm 0.42$. The value of N obtained here for M8 is comparable with that obtained for the Serpens (Harvey et al. 2006) and North American Nebula (Guieu et al. 2009) star forming regions, indicating the similarity of ages of these regions.

Fig 2 shows the mid-infrared colour-colour diagram constructed from the IRAC photometry for [3.6]-[4.5] vs [5.8]-[8.0] colour. In this diagram we show the photospheric sources as black dots, and the Class 0/I, Class II and Class III sources as open circles, open triangles and open squares. Table 1 lists the Class 0/I sources while Table 2 gives the Class II sources. Also included in Table 1 is the source KS 4 (No. 26; classified as YSO by Arias et al. (2006)) for which IRAC has detections in Chs. 1 & 2 only. Where available, the colours [J-H] and [H-K] along with the H magnitude from JHK surveys are also given in the Tables with references.

In order to obtain quantitatively the spatial distribution of YSOs, we adopted the nearest-neighbour technique (see Chavarria et al. (2008); Guieu et al. (2009); Evans et al. (2009)). We have followed the suggestion of Casertano & Hut (1985) to obtain surface density distribution, without a bias towards over-estimation. We used a 5 arcsec grid to compute the surface number density, defined

as $\rho_n = (n - 1)/A_n$, where A_n is the surface area defined by the radial distance r_n to the n ($= 5$) nearest-neighbours. Fig 3 shows the YSO spatial density contours with the inner and outer contours representing 10 and 5 YSOs/pc² respectively. The maximum densities are about 20 YSOs/pc². Also shown in the figure are the spatial distributions of all the 327 YSOs (a) and the contaminants (b). One can notice in Fig 3 several small clusters (about 7) isolated by the technique used as above. These clusters are mostly confined to the Hourglass, NGC 6530, M8E and the ridge regions along with two more clumps east of H36. In order to identify the cluster members as against the isolated or scattered cases, we computed the empirical cumulative distribution as a function of nearest-neighbour distance and found that the sources within an arbitrarily chosen inflection distance d_c (that signifies the maximum separation between the cluster members) of ~ 0.75 pc (0.03° at 1.25 kpc). By varying d_c between 0.65 and 0.85 pc, the number of cluster members does not change significantly. The Class 0/I and Class II YSOs in clusters constitute about 60% of the total number detected and are confined mainly within the YSO density contours (corresponding to about 7 clusters) shown in Fig 3. In comparison, only about 26 % of the Class III sources (having ‘‘anemic’’ disks) occur in the clusters. The ratio N mentioned before varies from cluster to cluster with an average of 2.29 which is comparable to the one for the entire sample (2.63) within the Poisson errors. It may be noted here that the surface density of YSOs derived by us is very close to the values obtained for star forming regions elsewhere (see Billot et al. (2010) and references therein).

It may be noted here that since M8 ($l = 5.958$; $b = -1.167$) is located near the mid-plane of the Galaxy, there exists a possibility of our YSO sample being still contaminated from other intrinsically ‘‘red sources’’, such as AGB stars. Recently Robitaille et al. (2008) prepared an extensive catalogue of such red sources based on the *Spitzer* GLIMPSE and MIPS GAL surveys. While the best way to distinguish between YSOs and AGB stars is by spectroscopy, these authors showed that the two classes are well separated in the [8.0-24.0] colour space, YSOs being redder than AGB stars in this space (see also Whitney et al. (2008)). Since in the present case of M8 we do not have the 24 μm data (from MIPS), we have estimated the AGB contamination by using the criteria based on the IRAC magnitudes and colour space (Robitaille et al. 2008). Since AGB stars are unlikely to occur in clusters, we have removed the clustered YSOs from our estimates. We find that our Class 0/I and II samples may be contaminated by AGB stars up to about 19%, while we do not find any contamination for our Class III sources. As pointed out by Robitaille et al. (2008), these separation criteria (including [8.0-24.0] colour) are ‘‘only approximate and there is likely to be contamination in both directions’’.

Fig 4 shows Ch3 (5.8 μm) image overlaid by the IRAC Class 0/I (open circles) and Class II (open triangles) sources identified by using the α_{IRAC} criteria (see Tables 1 and 2). Also shown (as black star symbols) in the figure are the positions of sub-mm (850 μm) gas clumps (taken from Table 1 of Tothill et al. (2008)). The YSO density contours (in white) are also shown in the figure. A number of the Class 0/I and Class II sources occur very close to the dense filamentary/pillar-like structures seen all along the ridge region in the east-west direction as well as perpendicular to

it in the central ridge or NGC 6530 region (see Fig 1). A majority of these sources are found to be present in the vicinity of the sub-mm gas clumps (marked by black star symbols in Fig 4). As mentioned earlier, M8E is a young compact high-mass star forming region. The central source of this cluster was resolved into a protostar M8E-IR and M8E-Radio, a B2 type star that is responsible for the compact HII region (Simon et al. 1984). While IRAC bands are saturated for M8E-IR itself, about 6 Class I or flat-spectrum and 10 Class II sources are identified by IRAC in a region of 4 arcmin² around M8E. These sources are not common with those listed in Table 6 of Tothill et al. (2008). We did not find any IRAC pre-main-sequence sources in the vicinity of the source IRAS 18014-2428, believed to be another young star forming region (corresponding to the sub-mm gas clump called SE3 (Tothill et al. 2002)).

Triggered star formation by the “collect and collapse” process (Elmegreen & Lada 1977) could be responsible for the existence of the IRAC sources, possibly started by the stellar winds or expanding HII regions associated with the nearby massive stars, viz. HD 165052, M8E, HD 164806, HD 164816, 9 Sgr and Her 36 (see Tothill et al. (2002)). While the ionization fronts from 9 Sgr and Her 36 have expanded well into the molecular cloud, that from M8E seems to have started later, as is evident from the bright narrow rim in front of M8E seen in Fig 1. Thus the small cluster in M8E region may be younger than others in the region. Linz et al. (2009) modelled the spectral energy distribution of M8E-IR and concluded that it is a B0 type YSO. That the star formation is sequential in M8 starting from north-west regions to southern edge regions has been shown by Damiani et al. (2004), based on Chandra X-ray survey of NGC 6530 region and its neighbourhood in conjunction with 2MASS data and optical surveys (see Tothill et al. (2008) for a discussion).

3.2 IRAC Ratio Maps

As mentioned earlier, the IRAC bands contain a number of prominent molecular lines/features. Ch1 contains H₂ vibrational-rotational lines while Ch2-4 mostly contain pure rotational lines. Ch1, 3 and 4 also contain the PAH features at 3.3, 6.2, 7.7 and 8.6 μm ; but Ch2 does not include any PAH features. In addition to these molecular lines/features, IRAC bands also contain hydrogen recombination lines, notably the Br α line (4.05 μm) in Ch2, which can be used to trace HII regions. Several authors have utilised the ratios of IRAC bands to identify some of the atomic and molecular diagnostics mentioned above (e.g., Smith & Rosen (2005); Povich et al. (2007); Neufeld & Yuan (2008)). Since it is difficult to assess the contribution of different atomic or molecular transitions to different channels, the ratio maps are only indicative; until/unless supplemented by spectroscopic evidence.

The Ch2 is more sensitive to H₂ lines of high excitation temperatures while the Ch4 represents rotational lines of low excitation temperatures (Neufeld & Yuan 2008). Likewise, the Ch2 does not have any PAH features while Ch4 has. Thus, in the ratio image of Ch2/Ch4, the brighter regions indicate emission regions from higher excitations from H₂ and the darker regions indicate PAH emission. This trend is reversed in the image of Ch4/Ch2 (i.e., bright regions show PAH emission and dark regions the H₂ emission). However

in HII regions, the H recombination lines (Br α and Pf β) are more significant contributors to Ch2 rather than the H₂ lines.

In order to make the ratio maps, point sources from all the IRAC images are removed by using an extended aperture of 12.2 arcsec and sky annulus of 12.2-24.4 arcsec in IRAF/DAOPHOT software (Reach et al. 2005). Then these residual frames are subjected to median filtering with a width of 15 pixels and smoothing by 3 \times 3 pixels using “box-car” algorithm (Povich et al. 2007). Fig 5a gives the ratio map of Ch2/Ch4 in a region of 0.67 \times 0.46 pc² around Her 36. Contours overlaid on the ratio map represent the H α emission observed by HST (in F656N filter image extracted from HST public archive). The minimum and maximum values of the contours are 5288 and 14100 counts respectively; six contours are drawn with interval of 1762 counts. In the vicinity of Her 36 the ratio map Ch2/Ch4 shows bright regions coinciding very nicely with the Hourglass HII region (as traced out by the contours of H α). The bright regions coinciding with the Hourglass can not be attributed to the molecular hydrogen lines of higher excitation temperature present in Ch2 in comparison with those of lower excitation temperature present in Ch4 (see Smith & Rosen (2005)). Further, the molecular hydrogen (1-0 S(1) at 2.12 μm) images presented by Burton (2002) do not show substantial emission around the Hourglass region (refer Figs 3 and 4 of Burton (2002)). Considering the fact that the IRAC Ch2 also contains Hydrogen Br α line (as well as Pf β (4.65 μm)), we may attribute the bright regions in the ratio map of Ch2/Ch4 coinciding with Hourglass, as due to Br α (and Pf β) emission. One can notice narrow bright regions surrounding Her 36 (and the near-IR source KS1) in the ratio map of Ch2/Ch4. These regions are coincident with those of molecular hydrogen in Burton (2002). In these regions it is likely that the molecular hydrogen transitions of high excitation temperature may be responsible rather than Br α . A similar trend is seen in the ratio image of Ch2/Ch3 also. Fig 5b gives the ratio image Ch4/Ch2 in the same region as in Fig 5a. In this figure, the ratio contours are overlaid on ratio image for better clarity and insight. One can notice a bright (corresponding to dark region in Fig 5a) “cavity”-like structure to the east of the Hourglass. Actually, this structure occurs towards the east of the regions of very high column density reported by Arias et al. (2006) towards north and east of the Hourglass. It is possible that the PAH molecules can be shielded from high energy UV photons by these dense regions. But the molecules may be excited by the low energy (non-ionising) UV photons that can escape from the narrow dense regions between the Hourglass and the “cavity”. Thus we may attribute the bright tubular structure to PAH emissions.

It may be mentioned here that the ratio image of Ch2/Ch1 does not show the Hourglass as prominently as in Ch2/Ch4 or Ch2/Ch3. This could be because of the fact that Ch1 contains Pf γ (3.7 μm) and Pf δ (3.3 μm) lines which may be cancelling partly the recombination lines in Ch2. In fact we do clearly see the Hourglass HII region in the ratio images of Ch1/Ch3 and Ch1/Ch4 also. Thus the Ch1 and Ch2 bring out well the H recombination emission in the Hourglass. Ch4 is unable to depict the HII region in spite of the presence of Pf α (7.5 μm), mainly because of the fact that its spectral response is inferior to that of Ch1 (or that

of Ch2) (Smith & Rosen 2005). For a HII region under Case B situation (Hummer & Storey 1987) with a kinetic temperature of 10^4 K and electron densities of 10^2 - 10^6 cm^{-3} , the combined relative intensities of $\text{Pf}\gamma$ and $\text{Pf}\delta$ are a factor of ~ 1.4 times lower than that of $\text{Pf}\alpha$. Hence the combined detected flux of $\text{Pf}\gamma$ and $\text{Pf}\delta$ in Ch1 can exceed that of $\text{Pf}\alpha$ in Ch4.

Elsewhere in M8 the ratio maps seem to have a different story to tell. Fig 6 gives the ratio maps of the ridge regions in M8 complex in an area of 24.2×20.0 arcmin², to the east/south-east of Her 36: Ch1/Ch2 (top), Ch3/Ch2 (middle) and Ch4/Ch2 (bottom). The ratio images show bright rims corresponding to the filamentary structures all along and perpendicular to the east-west ridge region. These regions seem to be bright in all bands, except Ch2 that is free of PAH features. Hence it is tempting to attribute the bright regions seen in the ratio images in Fig 6 to the PAH features. It is unlikely that these bright regions are a result of molecular hydrogen emission; since they occur in all the bands though at different excitation temperatures (mostly rotational lines) and should have cancelled each other in the ratio maps.

4 CONCLUSIONS

The important conclusions of this work are as follows:

(i) *Spitzer* IRAC photometry of M8 region revealed 64 Class 0/I and 168 Class II YSOs. About 60% of these are present in about 7 small clusters with spatial surface densities of 10-20 YSOs/pc²;

(ii) These sources are positioned close to the sub-mm gas clumps and the filamentary or pillar like structures present in M8. It is possible that the formation of these sources could have been triggered by stellar winds or expanding HII regions associated with the massive stars in the region;

(iii) The ratio map Ch2/Ch4 reveals $\text{Br}\alpha$ emission corresponding to the Hourglass HII region powered by Her 36 and its inverted ratio (Ch4/Ch2) identifies PAH emission in a cavity, east of the Hourglass;

(iv) The ratio maps Ch1/Ch2, Ch3/Ch2 and Ch4/Ch2 indicate the presence of PAH emission in both the ridges oriented along E-W and NE-SW directions.

ACKNOWLEDGMENTS

The research work is supported by the Department of Space, Government of India at PRL. This work is based (for a large part) on observations made with the Spitzer Space Telescope, which is operated by the Jet Propulsion Laboratory, California Institute of Technology under a contract with NASA. We acknowledge the use of data from the 2MASS, which is a joint project of the University of Massachusetts and the Infrared Processing and Analysis Center/California Institute of Technology, funded by the NASA and the NSF. The authors sincerely appreciate the very useful comments from the anonymous referee.

REFERENCES

- Allen D. A. 1986, MNRAS, 319, 35P
 Allen L. E. et al., 2004, ApJS, 154, 363
 Arias J. I., Barba R. H., Maiz Apellaniz J., Morrell N. I. and Rubio M., 2006, MNRAS, 366, 739
 Arias J. I., Barba R. H., Morrell N. I. 2007, MNRAS, 374, 1253
 Barba R. H. and Arias J. I., 2007, A&A, 471, 841
 Bessell M. S. and Brett J. M., 1988, PASP, 100, 1134
 Billot N., Noriega-Crespo A., Carey S., Guieu S., Shenoy S., Paladini R., Latter W., 2010, ApJ, 712, 797
 Brand P. W. J. L. and Zealey W. J., 1978, A&A, 63, 345
 Burton M. G., 2002, PASA, 19, 260
 Casertano S., & Hut P., 1985, ApJ, 298, 80
 Chavarria L. A., Allen L.E., Hora J. L., Brunt C. M., and Fazio G. G., 2008, ApJ, 682, 445
 Crowther P. A. and Conti P. S., 2003, MNRAS, 343, 143
 Damiani F., Flaccomio E., Micela G., Sciortino S., Harnden F. R., Jr., Murray S. S., 2004, ApJ, 608, 781
 Elmegreen B. G., and Lada C. J., 1977, ApJ, 214, 725
 Evans II N. J., et al., 2009, ApJSS, 181, 321
 Fazio G. G. et al., 2004, ApJS, 154, 10
 Flaherty K. M., Pipher J. L., Megeath S. T., Winston E. M., Gutermuth R. A., Muzerolle J., Allen, L. E., and Fazio, G. G., 2007, ApJ, 663, 1069
 Goudis C., 1976, Ap&SS, 40, 281
 Greene T. P., Wilking B. A., Andre P., Young E.T., and Lada C. J., 1994, ApJ, 434, 614
 Guieu S., et al., 2009, ApJ, 697, 787
 Gutermuth R. A., et al., 2008, ApJ, 674, 336
 Gutermuth R. A., Megeath S. T., Myers P. C., Allen L. E., Pipher J. L. and Fazio G. G., 2009, ApJSS, 184,18
 Harvey P. M., et al., 2006, ApJ, 644, 307
 Harvey P. M., Merin B., Huard T. L., Rebull L. M., Chapman N., Evans II N. J., and Myers P. C., 2007, ApJ, 663, 1149
 Hummer D. G., and Storey P. J., 1987, MNRAS, 224, 801
 Lada C. J. and Adams F. C., 1992, ApJ, 393, 278
 Lada C. J., Gull T. R., Gottlieb C. A. and Gottlieb E. W., 1976, ApJ, 203, 159
 Lada C.J., et al., 2006, AJ, 131, 1574
 Linz H. et al., 2009, A&A, 505, 655
 Lynds B. T., and O'Neil E. J.Jr., 1982, ApJ, 263, 130
 Makovoz D., and Marleau F. R., 2005, PASP, 117, 1113
 Megeath S. T. et al., 2004, ApJS, 154, 367
 Meyer M. R., Calvet N. and Hillenbrand L. A., 1997, AJ, 114, 288
 Mitchell G. F., Maillard J.-P., Hasegawa T. I., 1991, ApJ, 371, 342
 Muench A. A., Lada C. J., Luhman K. L., Muzerolle J., and Young E., 2007, AJ, 134, 411
 Neufeld D. A. and Yuan Y., 2008, ApJ, 678, 974
 Povich M. S. et al., 2007, ApJ, 660, 346
 Reach W. T., et al. 2005, PASP, 117, 978
 Robitaille T. P., et al. 2008, AJ, 136, 2413
 Simon M., Cassar L., Felli M., Fischer J., Massi M. and Sanders D., 1984, ApJ, 278, 170
 Skrutskie, M. F. et al. 2006, AJ, 131, 1163
 Smith M. D. 2004, The Origin of Stars, Imperial College Press, London, p. 123
 Smith, M. D., and Rosen, A., 2004, MNRAS, 357, 1370

- Stecklum B., Henning T., Eckart A., Howell R. R. and Hoare M. G., 1995, ApJ, 445, L153
- Stecklum B., Henning T., Feldt M., Hayward T. L., Hoare M. G., Hofner P. and Richter S., 1998, AJ, 115, 767
- Tothill N. F. H., Gagne M., Stecklum B., Kenworthy M. A., 2008, Handbook of Star Forming Regions Vol II, Astron. Soc. Pacific, Ed. B. Reipurth
- Tothill N. F. H., White G. J., Matthews H. E., McCutcheon W. H., McCaughrean M. J. and Kenworthy M. A., 2002, ApJ, 580, 285
- White G. J., Tothill N. F. H., Matthews H. E., McCutcheon W. H., Hultgren M., and McCaughrean M. J., 1997, A&A, 323, 529
- Whitney B. A., et al. 2008, AJ, 136, 18
- Woodward C. E. et al., 1986, AJ, 91, 870
- Woodward C. E., Pipher J. L., Helfer H. L., Forrest W. J., 1990, 365, 252
- Woolf, N. J. 1961, PASP, 73, 206
- Wright E. L., Lada C. J., Fazio G. G., Kleinmann D. E., Low F. J., 1977, AJ, 82, 132

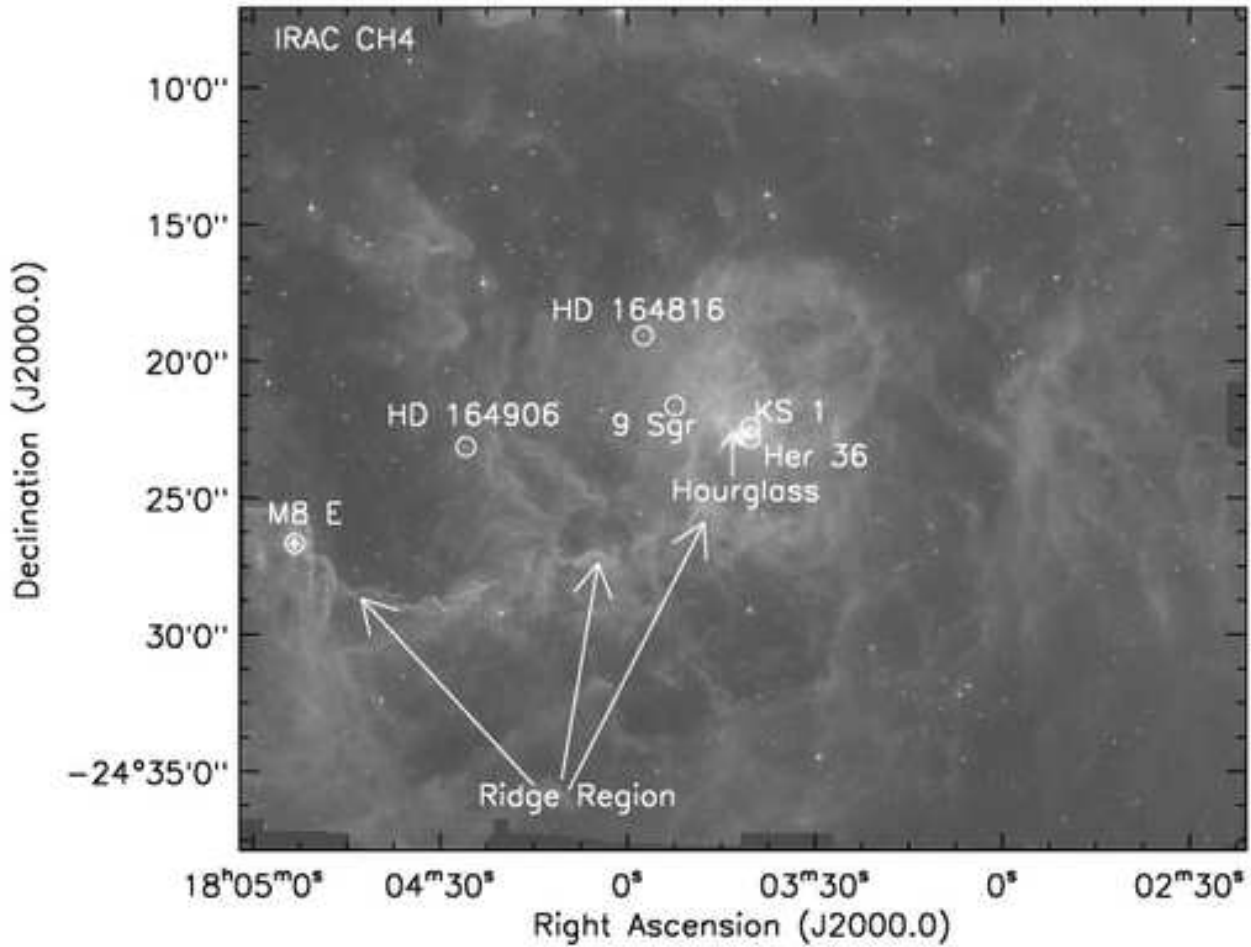


Figure 1. Spitzer IRAC Ch4 ($8.0 \mu\text{m}$) image of Lagoon Nebula region ($\sim 42.5 \times 30.0 \text{ arcmin}^2$). The locations of well known sources are shown circled: the massive O type stars Her 36 and 9 Sgr; the early B type stars HD 164906 and HD 164816; the near-infrared source KS1 just north of Her 36; and the young compact massive star-forming region M8E to the extreme east. The Hourglass HII region is shown by the arrow near the core of M8. The young cluster NGC 6530 is situated just to the west of the massive star HD 164906. The arrows at the bottom show the ridge region in the east-west direction. One can also notice filamentary features in the central ridge running north-south near the star HD 164906. The massive star HD 165052 is towards the east of M8E but it is not covered by the IRAC observations.

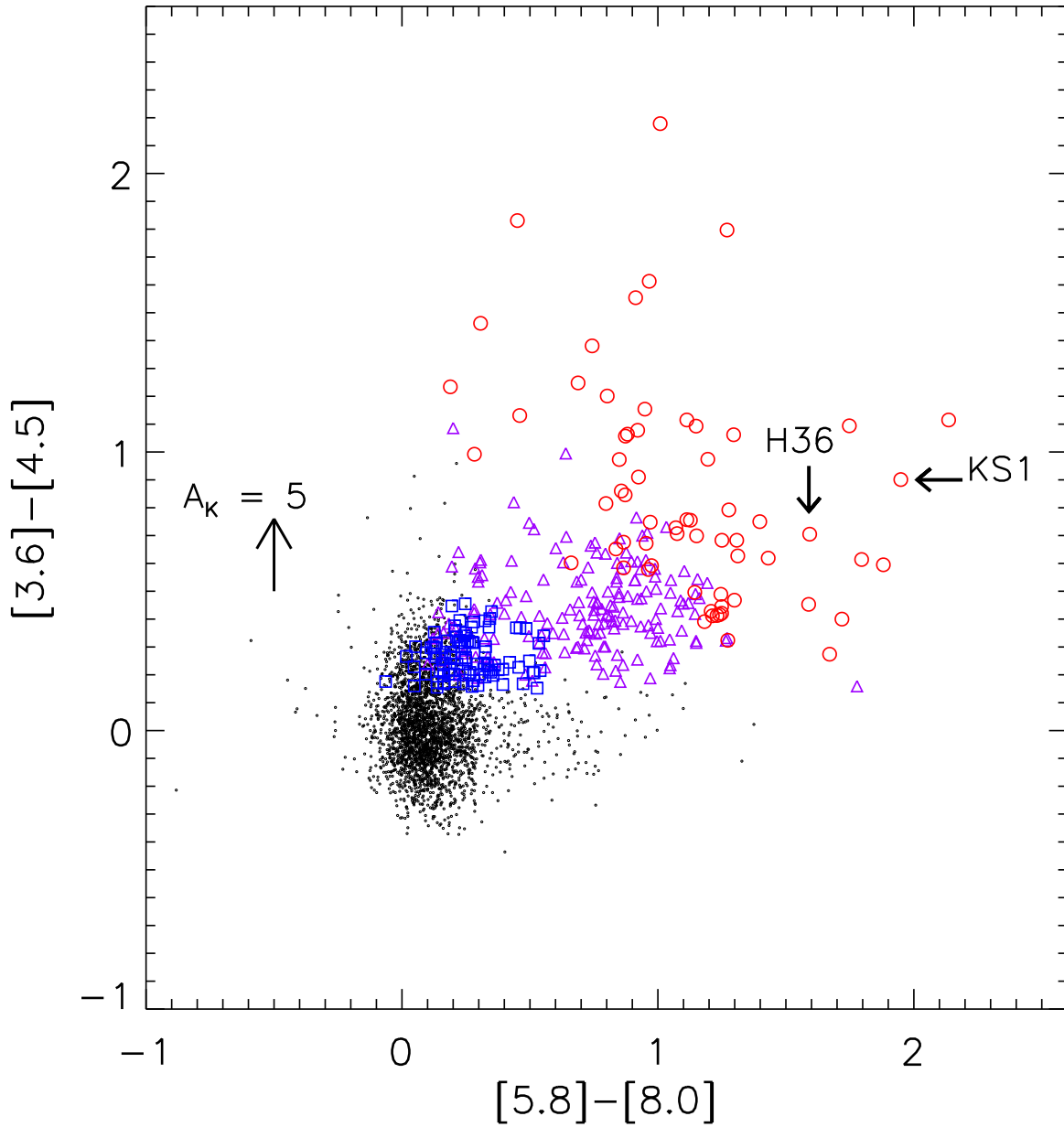
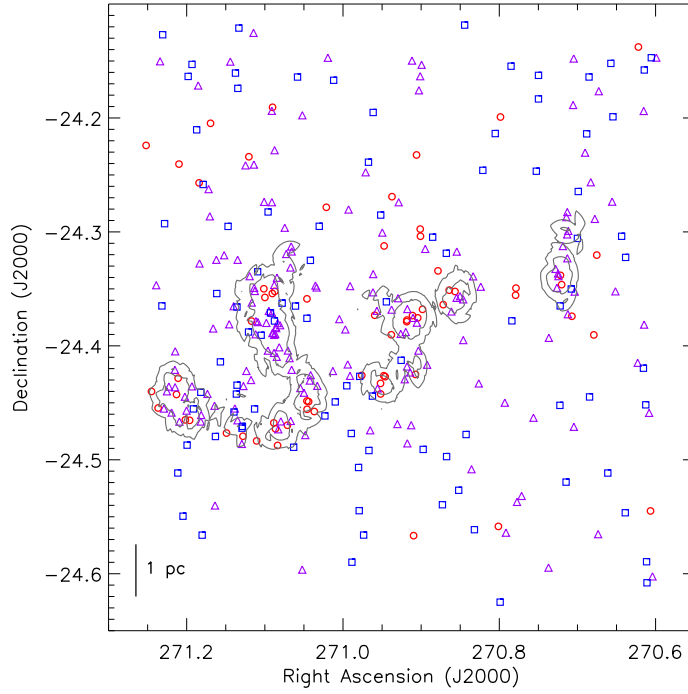
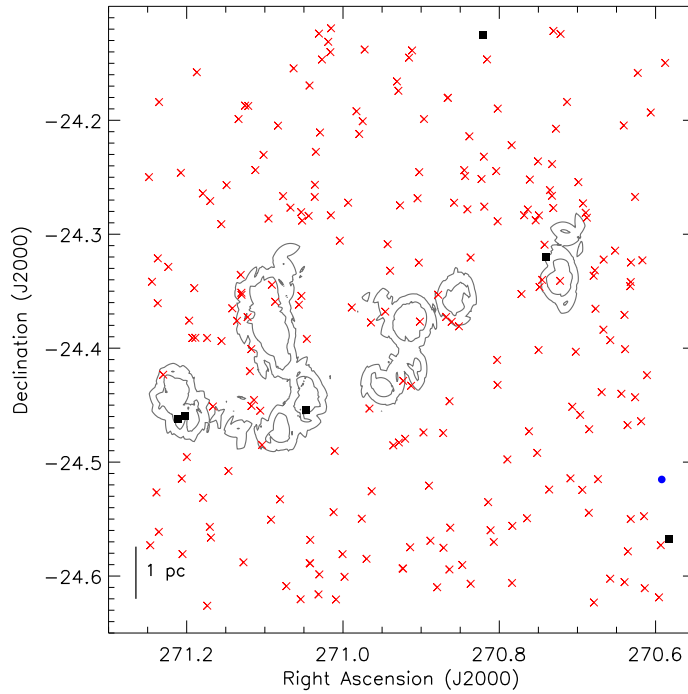


Figure 2. Mid-IR color-color diagram using the Spitzer IRAC bands for all the sources identified within the region shown in Fig 1. The sources KS1 and Her 36 are marked by arrows. The upward arrow on the left shows the extinction vector for $A_K = 5$ mag, using average extinction law from Flaherty et al. (2007). The black dots around the centre (0,0) locate the stars with only photospheric emissions. The open squares (blue), open triangles (violet) and open circles (red) represent respectively, Class III, Class II and Class 0/I sources, obtained from the α_{IRAC} criteria.



(a)



(b)

Figure 3. a: Spitzer IRAC field of M8 showing all the 327 YSOs: open circles (red) show Class 0/I sources, open triangles (violet) show Class II and open squares (blue) show Class III sources; b: Spitzer IRAC field of M8 showing contaminants: crosses (red) show unresolved PAH aperture contaminations, filled squares (black) show shocked emission knots and the lone filled circle (blue) the PAH galaxy contaminant. In both the figures, the contours show YSO iso-density at 5 (outer) and 10 (inner) YSOs/pc².

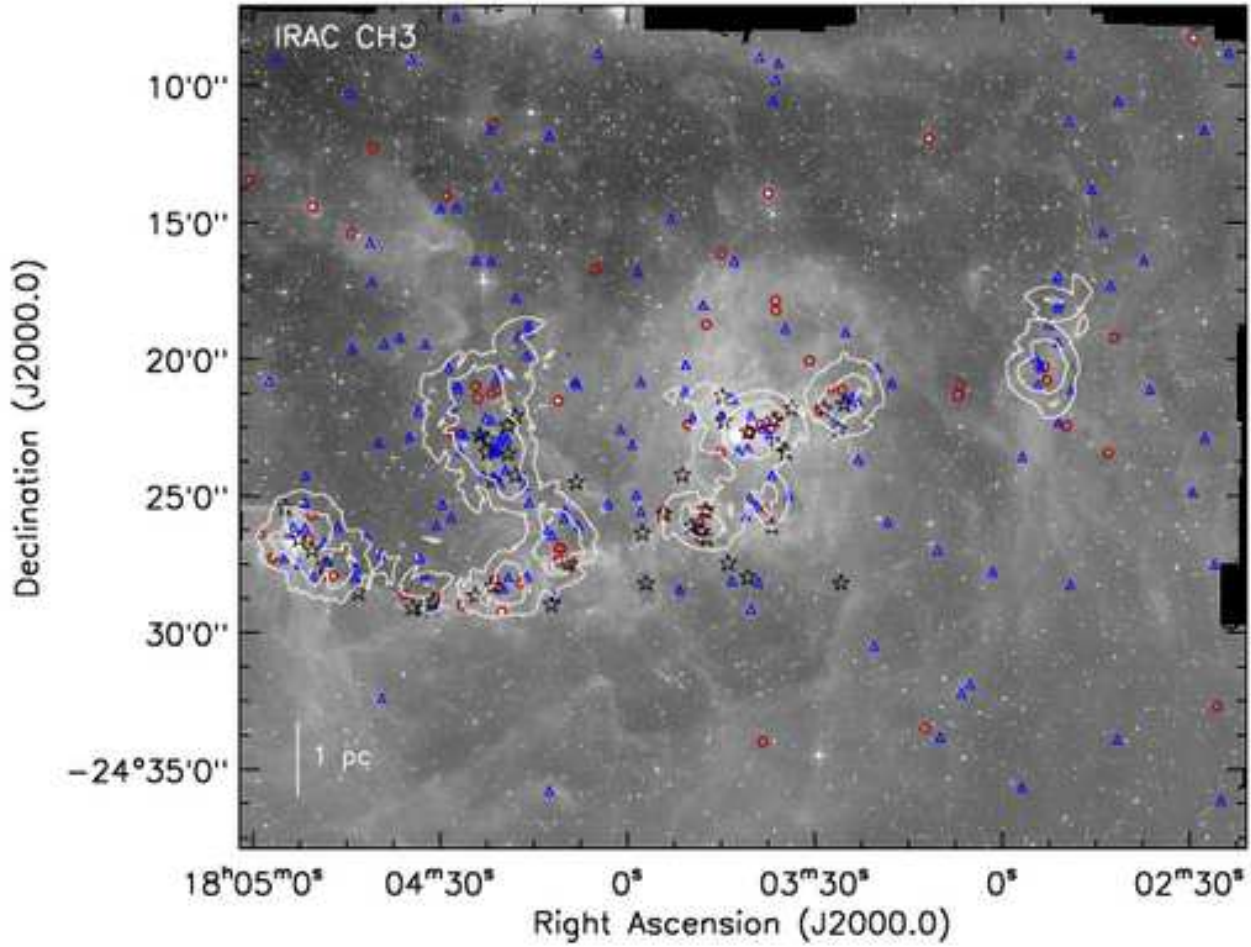
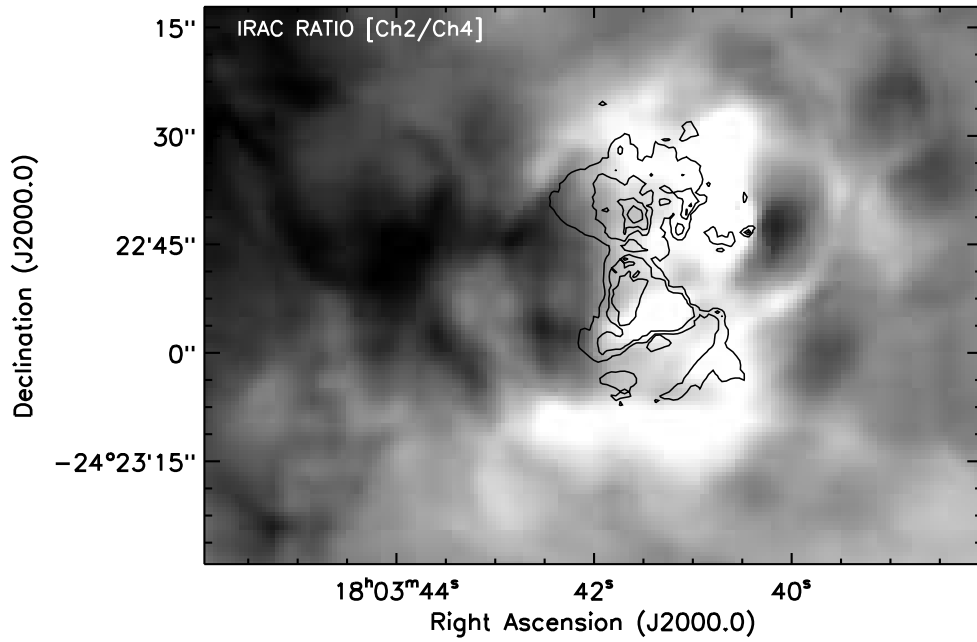
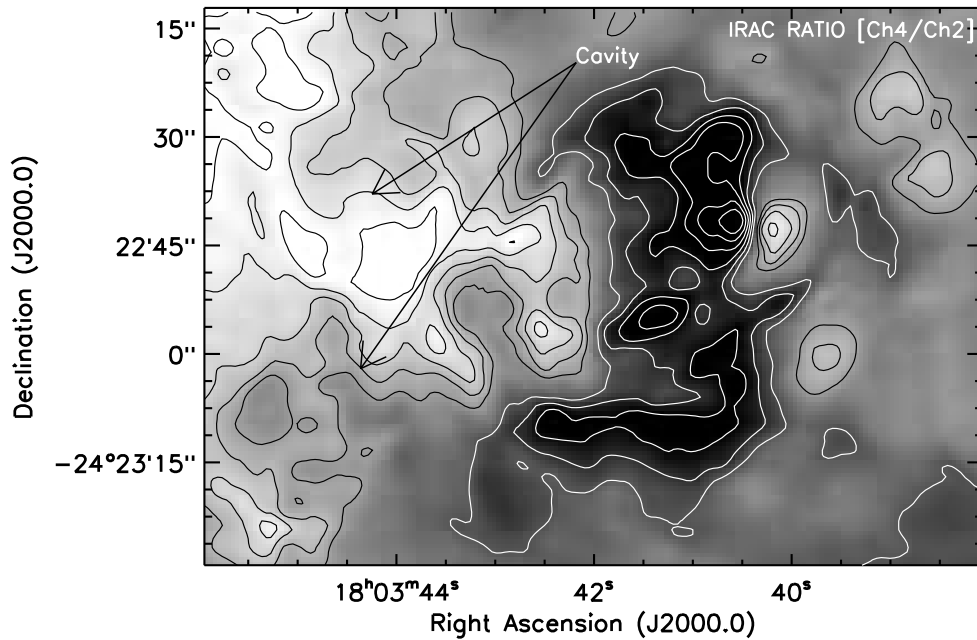


Figure 4. Spitzer IRAC Ch3 ($5.8 \mu\text{m}$) image of M8 ($\sim 42.5 \times 30.0 \text{ arcmin}^2$) superposed by IRAC Class 0/I and II sources and sub-mm gas clumps. The open circles (red) and open triangles (blue) show the IRAC Class 0/I and II sources respectively (from Tables 1 and 2 of the present work); the black star symbols represent the locations of the sub-mm gas clumps (from Table 1 of Tothill et al. (2008)). The overlaid contours (white) are YSO density contours generated using a grid size of 5 arcsec: the inner contours are 10 YSOs/pc^2 and the outer contours represent 5 YSOs/pc^2 .



(a)



(b)

Figure 5. a: Ratio image of Ch2/Ch4 of M8 (Lagoon Nebula) in log scale overlaid by HST H α (F656N filter) contours, in a region around Her 36 of size 110×76 arcsec². The contour levels are between 5288 and 14100 counts. The bright regions indicate the prominence of Ch2 over Ch4, while the dark regions have the reverse trend. The bright “3” shaped structure is more extended than the H α contours and nearly coincide with them. b: Ratio image of Ch4/Ch2 of M8 (Lagoon Nebula) in log scale. The bright regions indicate the prominence of Ch4 over Ch2. For better insight, the ratio image is overlaid by the ratio contours: the black contours in the bright regions represent ratio levels between 17.4 and 22.8; and the white contours in the dark regions indicate the ratio levels of 14.3 to 8.4. The region of possible PAH emission is the bright tubular structure within the “cavity”, seen east of the Hourglass.

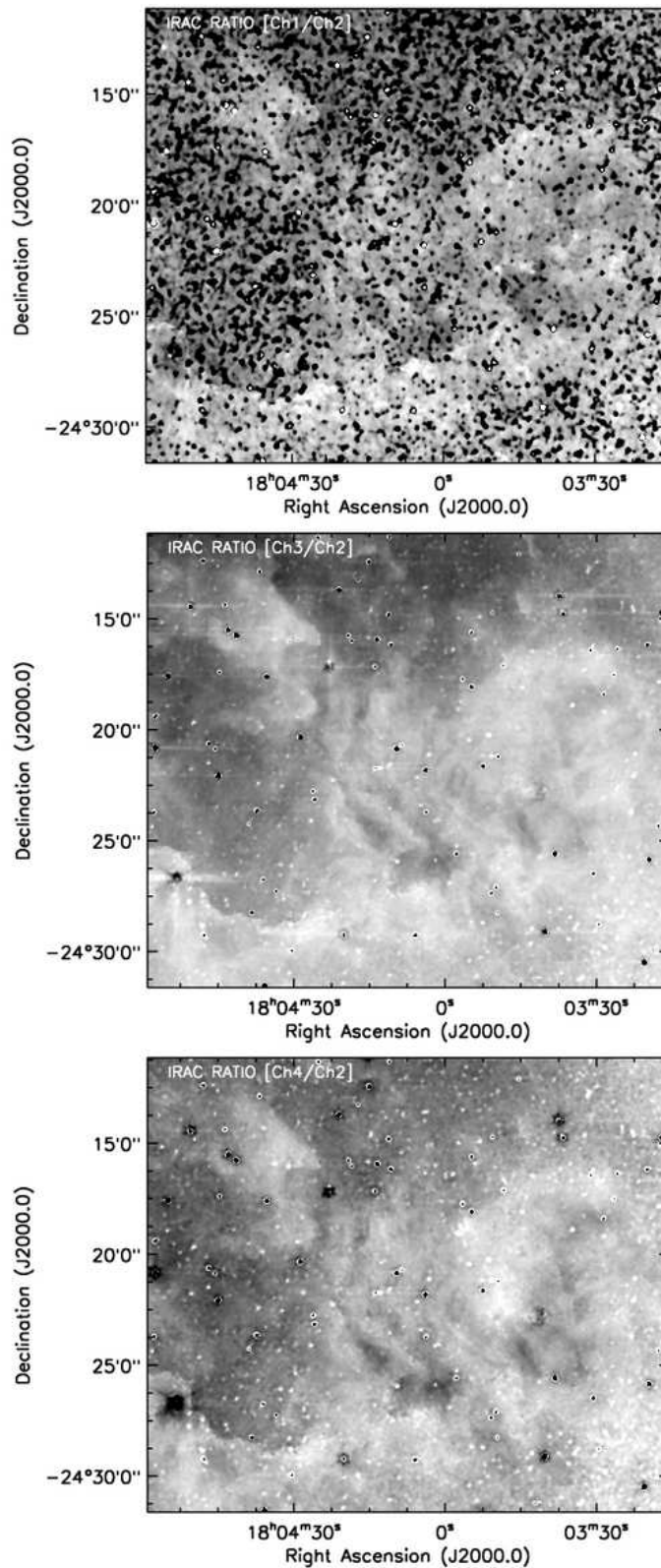


Figure 6. Ratio maps of Ch1/Ch2 (top), Ch3/Ch2 (middle) and Ch4/Ch2 (bottom) in log scale (in a region of size $\sim 24.2 \times 20.0$ arcmin²), showing the ridges and filamentary structures (towards east/south-east of Her 36). The dominance of Ch1, Ch3 and Ch4 (bright portions) over Ch2 in the ridge region and filamentary regions can be noticed, which may be attributed to the PAH emission in these regions. The black dots (seen mostly in Ch1/Ch2) and the white dots (seen mostly in Ch3/Ch2 and Ch4/Ch2) are the result of the residueing process.